



AMERICAN METEOROLOGICAL SOCIETY

Journal of Physical Oceanography

EARLY ONLINE RELEASE

This is a preliminary PDF of the author-produced manuscript that has been peer-reviewed and accepted for publication. Since it is being posted so soon after acceptance, it has not yet been copyedited, formatted, or processed by AMS Publications. This preliminary version of the manuscript may be downloaded, distributed, and cited, but please be aware that there will be visual differences and possibly some content differences between this version and the final published version.

The DOI for this manuscript is doi: 10.1175/JPO-D-16-0215.1

The final published version of this manuscript will replace the preliminary version at the above DOI once it is available.

If you would like to cite this EOR in a separate work, please use the following full citation:

Busecke, J., R. Abernathey, and A. Gordon, 2017: Lateral eddy mixing in the subtropical salinity maxima of the global ocean. *J. Phys. Oceanogr.* doi:10.1175/JPO-D-16-0215.1, in press.

© 2017 American Meteorological Society



1 Lateral eddy mixing in the subtropical salinity maxima of the global ocean

2 Julius Busecke*, Ryan P. Abernathey and Arnold L. Gordon

3 *DOCP, LDEO, 61 Route 9W, Palisades, NY USA.*

PRELIMINARY ACCEPTED VERSION

4 *Corresponding author address: DOCP, LDEO, 61 Route 9W, Palisades, NY USA.

5 E-mail: julius@ldeo.columbia.edu

ABSTRACT

6 A suite of observationally driven model experiments is used to investigate
7 the contribution of near-surface lateral eddy mixing to the subtropical sur-
8 face salinity maxima in the global ocean. Surface fields of salinity are treated
9 as a passive tracer and stirred by surface velocities derived from altimetry,
10 leading to irreversible water mass transformation. In the absence of surface
11 forcing and vertical processes, the transformation rate can be directly related
12 to the integrated diffusion across tracer contours, which is determined by the
13 observed velocities. The destruction rates of the salinity maxima by lateral
14 mixing can be compared to the production rates by surface forcing, which act
15 to strengthen the maxima. The ratio of destruction by eddy mixing in the sur-
16 face layer versus the surface forcing exhibits regional differences in the mean
17 - from 10% in the South Pacific up to 25% in the South Indian. Furthermore,
18 the regional basins show seasonal and interannual variability in eddy mixing.
19 The dominant mechanism for this temporal variability varies regionally. Most
20 notably, the North Pacific shows large sensitivity to the background salinity
21 fields and a weak sensitivity to the velocity fields while the North Atlantic
22 exhibits the opposite behavior. The different mechanism for temporal vari-
23 ability could have impacts on the manifestation of a changing hydrological
24 cycle in the SSS field specifically in the North Pacific. We find evidence for
25 large scale interannual changes of eddy diffusivity and transformation rate in
26 several ocean basins that could be related to large scale climate forcing.

27 **1. Introduction**

28 The terrestrial freshwater cycle and its behavior in a changing climate is a study area of utmost
29 importance to humanity, specifically from a socio-economic viewpoint (Durack 2015). Due to the
30 interconnection of various branches of the water cycle and the vastly larger size of the ocean reser-
31 voir relative to the land surface (Durack 2015; Schmitt 2008) understanding the oceanic branch
32 might be key in improving our understanding of how a changing climate will influence the terres-
33 trial water cycle.

34 Studying the freshwater flux over the ocean is very challenging due to complicated and spatially
35 sparse measurements and the reliance on bulk formulas for various flux products, resulting in
36 large uncertainties between data sets (Schanze et al. 2010). Due to these difficulties, the idea
37 of using sea surface salinity (SSS) as a proxy of the integrated freshwater forcing has emerged
38 (Schmitt 2008; Gordon and Giulivi 2008). By removing (adding) freshwater through evaporation
39 (E) (precipitation (P)) at the surface the SSS is raised (lowered). The general alignment between
40 the areas of positive net evaporation (evaporation - precipitation) and local salinity maxima in the
41 subtropical gyre of the North Atlantic was pointed out as early as (Wüst 1936). The complication
42 with this approach, often called “salinity as an ocean rain gauge” (Schmitt 2008), is the influence
43 of ocean dynamics (Vinogradova and Ponte 2013; Ponte and Vinogradova 2016; Gordon 2016).

44 The SSS distribution is influenced by advection and mixing both horizontally and vertically, and
45 all processes need to be quantified in order to relate changes in the SSS field to changes in the
46 water cycle. To achieve this goal, the SPURS (Salinity Processes in the Upper Ocean Study) field
47 experiment was carried out in the SSS-maximum (SSS-max) of the subtropical North Atlantic,
48 with the goal to observe all relevant processes in one of the global salinity maxima and then apply

49 these findings to the other subtropical regions in the global ocean. An overview of the program
50 and many relevant publications is given by Lindstrom et al. (2015).

51 Besides being relevant for the study of the surface salinity expression of a change in the global
52 water cycle, the SSS-maxima are source regions for subtropical underwater (STUW, O'Connor
53 et al. (2005)) that feed into the shallow overturning circulation (e.g. Schott et al. (2004)). These
54 subducted water mass characteristics are important for the global climate since they contribute
55 significantly to global tracer transports (e.g. Boccaletti et al. (2005)). This results from the strong
56 circulation paired with strong near surface gradients, compared to the deep ocean. Hence changes
57 in mean gradients of temperature and salinity might modify meridional heat and freshwater trans-
58 ports of the upper ocean. Additionally the subducted water masses are a potential pathway for
59 subtropical surface anomalies to the tropical thermocline and subsequently the upwelling regions
60 of the globe. Changes in surface salinity on isopycnals are by definition associated with tempera-
61 ture (spice) anomalies which have the potential to alter sea surface temperature once upwelled in
62 the tropics. This emphasizes the need to study the mechanisms responsible for the variability of
63 the SSS.

64 Observations during SPURS show strong lateral salinity gradients associated with mesoscale
65 filaments. These gradients are most intense near the surface and the salinity variability is strongly
66 reduced along the subduction path of the SSS-max (Busecke et al. 2014). Motivated by these
67 findings, this study focuses on the process of lateral eddy mixing within the mixed layer. The
68 importance of eddy mixing to the mean salinity and volume budgets in the North Atlantic has
69 been covered in various studies (Gordon et al. 2015; Busecke et al. 2014; Bryan and Bachman
70 2014; Schmitt and Blair 2015; Johnson et al. 2016; Amores et al. 2016) using different methods
71 and data sources. When the destruction of the saltiest water masses is compared to the creation by
72 positive net evaporation, the studies infer different mean values and temporal variability.

73 We introduce a novel approach to estimate the eddy mixing contribution in all subtropical basins
74 with a coherent methodology. A suite of observation driven experiments is conducted where the
75 mechanism of water mass destruction via eddy mixing is isolated. Using a salinity coordinate
76 system, as in the pioneering study of (Walsh 1977), we investigate all major ocean basins. To-
77 gether with the comparison of the mean effect of eddy mixing for the SSS-max, we examine the
78 variability induced by the observed surface velocity field and test the sensitivity to seasonal and in-
79 terannual variations in SSS fields. These sensitivity experiments enable us to identify the dominant
80 processes for the variability in eddy mixing—the surface velocities or the SSS fields.

81 The manuscript is structured as follows: In the remainder of the introduction we address the
82 discrepancies within the existing estimates with a brief overview of the existing studies estimating
83 the relevance of eddy mixing to the North Atlantic SSS-max and discuss potential sources for
84 disagreement. Then we introduce the methodology, model set up and data used for this study in
85 section 2. We present and discuss the results in section 3 and conclude in section 4, including
86 possible future work.

87 *a. Budgets and the choice of a control volume*

88 In order to evaluate the importance of any process to a large-scale feature like the SSS-max, it
89 is useful to investigate the salinity budget over a control volume that encompasses the feature of
90 interest.

91 We start with the local salinity budget in a very general form.

$$\frac{\partial S}{\partial t} = -\nabla \cdot (F_S) = -\nabla \cdot (F_{S,Diff} + F_{S,Adv}) \quad (1)$$

92 with the boundary condition

$$F_{S,Diff} = F_{Surface} \hat{\mathbf{k}} \quad \text{at} \quad z = 0 \quad (2)$$

₉₃ $\hat{\mathbf{k}}$ is the unit vector normal to the surface.

₉₄ Here F_S is the sum of all both diffusive ($F_{S,Diff}$) and advective ($F_{S,Adv}$) oceanic salinity fluxes,
₉₅ and $F_{Surface}$ is the effective salinity flux due to freshwater forcing at the surface:

$$F_{Surface} = S(E - P) \quad (3)$$

₉₆ E is generally larger than P in the subtropical basins (e.g. Schanze et al. (2010)), and no significant
₉₇ sources and sinks for salinity exist in the interior ocean. The SSS-max is surrounded by fresher
₉₈ waters in the horizontal and vertical, leaving the surface forcing as the only process that can lead
₉₉ to an increase in salinity. In order to maintain a steady state, the diffusive and advective fluxes
₁₀₀ have to be directed out of the high salinity region, balancing the surface forcing.

₁₀₁ An appropriate volume has to be defined over which to compare surface forcing to salinity flux
₁₀₂ divergence. The salinity budget within an arbitrary volume V hence can be written as:

$$\begin{aligned} \iiint_V \frac{\partial S}{\partial t} dV &= \iiint_V -\nabla \cdot (F_{S,Diff} + F_{S,Adv}) dV \\ &= - \iint_{\partial V} (F_{S,Diff} + F_{S,Adv}) \cdot \hat{\mathbf{n}} \partial V + \iint_A F_{Surface} dA \end{aligned} \quad (4)$$

₁₀₃ The second equality follows from the divergence theorem. The integrated salinity tendency can be
₁₀₄ related to the salinity flux through ∂V , the internal (oceanic) boundary of V and the surface flux
₁₀₅ integrated over the surface area A. The vector $\hat{\mathbf{n}}$ is the unit normal vector of V .

₁₀₆ Two general choices of volumes are used in the literature:

₁₀₇ 1. The Eulerian control box: Most studies use some variation of a box fixed in space. Either
₁₀₈ a local grid box (Busecke et al. 2014) or point measurement from a mooring (Farrar et al.
₁₀₉ 2015), zonally elongated boxes within the SSS-max (Gordon and Giulivi 2014) or a larger
₁₁₀ box around the SSS-max (Qu et al. 2011; Amores et al. 2016).

₁₁₁ 2. The “water mass” boundary: The studies of Bryan and Bachman (2014); Schmitt and Blair
₁₁₂ (2015); Johnson et al. (2016) and this study utilize a control volume ($V(S_0, t)$) bounded by a

surface of constant salinity S_0 . It can be shown that this eliminates the advection term from the salinity budget, leaving only diffusion (both lateral and vertical) as a possible compensation for the surface forcing (Walsh 1977; Marshall et al. 1999). The budget becomes

$$\iiint_{V(S>S_0)} \frac{\partial S}{\partial t} dV = - \iint_{\partial V(S=S_0)} (F_{S,Diff}) \cdot \hat{n} \partial V + \iint_{A(S>S_0)} (F_{Surface}) \cdot \hat{n} dA \quad (5)$$

Note that in this case the surface forcing is also evaluated on the same isohaline control surface. The salinity budget in V can be related to the time change in volume bounded by the same isohaline (Transformation Rate; *TFR*) (see Bryan and Bachman (2014) for full derivation):

$$TFR = \frac{\partial(V(S_0, t))}{\partial t} = \frac{\partial}{\partial S_0} \iiint_{V(S>S_0)} \frac{\partial S}{\partial t} dV \quad (6)$$

In order to compare the results of the Eulerian and water-mass budgets, either the variability in the position of the control volume has to be negligible or the spatial variability of diffusive salinity fluxes and surface forcing must be very homogeneous in space. We argue that these conditions are not met.

The SSS-max exhibits variability from seasonal (Gordon and Giulivi (2014); Gordon et al. (2015)) to interannual (Bingham et al. 2014) to decadal (Gordon and Giulivi 2008; Durack and Wijffels 2010) time scales. Furthermore there is evidence for strong spatial variability of lateral diffusivities and SSS gradients (Abernathy and Marshall 2013; Gordon et al. 2015), implying strong spatial variability of the resulting diffusive fluxes. This could explain some of the spread of results between the studies using fixed control volumes. In the presence of strong inhomogeneity, even small differences in the position of the control volume will lead to very different results for each of the terms in the salinity/volume budget. Besides the choice of the control volume, a second major factor is the actual quantification of each of the terms in the budget. We focus our study

¹³³ on a particular process–lateral eddy mixing in the near-surface layer–and proceed by reviewing
¹³⁴ common methods to quantify this process.

¹³⁵ *b. Quantifying eddy mixing*

¹³⁶ In this section we outline the exact processes we aim to study in detail with respect to the SSS-
¹³⁷ max.

¹³⁸ Unsteady motions in the ocean play a large role for the general circulation, tracer transports and
¹³⁹ thereby global climate. Fox-Kemper et al. (2013) provides a review of mesoscale eddy transport
¹⁴⁰ in the ocean. Following their terminology, all fluctuations from the mean circulation with time
¹⁴¹ scales of weeks and length scales of several hundred kilometers (i.e. mesoscale) will be referred
¹⁴² to as “eddies.”

¹⁴³ Tracer fluxes caused by eddies are commonly expressed as a covariance term $\overline{\mathbf{u}'C'}$, where the
¹⁴⁴ primes indicate a deviation from the time mean represented by the over bar, such that $C = C' + \bar{C}$.

¹⁴⁵ A common approach is to represent the eddy flux using a diffusive closure involving the the
¹⁴⁶ mean tracer gradient and a tensor **R**:

$$\overline{\mathbf{u}'C'} \simeq -\mathbf{R}\nabla\bar{C} . \quad (7)$$

¹⁴⁷ However, here **R** does not represent a purely diffusive process. The tensor can be split up into a
¹⁴⁸ symmetric diffusion tensor (**K**) and an asymmetric advection tensor (e.g. Fox-Kemper et al. (2013)
¹⁴⁹ equation 8.25). Observational estimates of the diffusivity tensor are rare and usually derived from
¹⁵⁰ long term averages, and it is difficult to match such data sets to tracer fields to obtain an estimate
¹⁵¹ of the diffusive eddy flux, let alone resolve the diffusive flux into the SSS-max in time. For further
¹⁵² details and references on this approach the reader is referred to (Fox-Kemper et al. 2013) and
¹⁵³ references therein.

154 In order to circumvent these issues, we choose to simulate the evolution of surface tracer fields
155 using observed surface velocities and diagnose the diffusive flux within a coordinate system de-
156 fined by a water mass (here salinity). As illustrated in Fig. 1b and c, in a tracer coordinate system,
157 advective stirring by eddies stretches and filaments tracer contours, leading to irreversible mixing
158 (a.k.a. water mass transformation) at small scales and a net diffusive flux across tracer contours.
159 In this context, and throughout our study, “eddy mixing” refers to the enhancement of small-scale
160 mixing by mesoscale stirring (Figure 1).

161 To further separate the effects of the large scale tracer gradients and velocity we employ the
162 concept of “effective diffusivity” (Nakamura 1996). This diffusivity is appropriate for our anal-
163 ysis since it does not correspond to an Eulerian diffusivity, but rather represents the averaged
164 enhancement of small scale diffusivity along a tracer contour. Thus it is directly relevant to the net
165 diffusive flux across isohalines and into the SSS-max.

166 2. Methods and Data

167 As stated above, when evaluating a volume bounded by a tracer surface, the flux across this
168 boundary can only be achieved by diffusion and the flux through the sea surface (Equation 5 and
169 6). The sum of these fluxes is directly related to the volume bounded by the isohaline.

170 Our approach is only focused on the near surface layer for several reasons. Firstly, the availabil-
171 ity of velocity data for over 20 years through altimetry enables us to conduct a data driven study on
172 eddy mixing, which is not possible with subsurface data at this point. Secondly, the strong lateral
173 gradients observed within the mixed layer of the North Atlantic SSS-max (Busecke et al. 2014)
174 point to the importance of the near-surface lateral eddy mixing versus the interior. Global inverse
175 mixing estimates (Groeskamp et al. 2017) support the idea of lateral near surface eddy mixing
176 being much stronger than along isopycnal mixing in the interior.

177 We simulate a 2D salinity field advected by observed velocities, without any other forcing. By
 178 eliminating all other processes, the evolution of the water mass volume is governed purely by
 179 lateral mesoscale stirring. If the contour is closed, the lateral diffusive flux, integrated along a
 180 tracer contour is now directly related to the area transformation rate.

$$TFR_A(S_0, t) = \frac{\partial}{\partial t} \iint_{\substack{(S \geq S_0)}} dA = - \int_{\partial A(S=S_0)} (F_{S,Diff}) \cdot \hat{n} dA \quad (8)$$

181 In order to compare these values with the climatological surface forcing to determine the impor-
 182 tance to the volume budget, they have to be scaled with a depth. We chose the mean mixed layer
 183 depth within an isohaline $\overline{MLD}(S_0)$ to focus on the variability of lateral mixing without masking
 184 the results with the temporal variability of the mixed layer depth. That variability is not small and
 185 certainly influences any full budget estimate. Large variability of the mixed layer depth can be
 186 seen in the NA (Busecke et al. 2014; Farrar et al. 2015). Here we want to specifically focus on the
 187 variability in lateral stirring processes, hence the choice of a constant depth.

$$TFR_{Eddy,V}(S_0, t) = TFR_{Eddy,A}(S_0, t) \overline{MLD}(S_0) \quad (9)$$

188 This can be seen as a special case of Equation 6, where V_{S_0} is the extruded contour of $S(x, y, t) = S_0$
 189 (see Figure 1a). The upper and lower boundary both have the boundary condition

$$F_{S,Diff} = 0 \quad at \quad z = 0 \quad and \quad z = \overline{MLD}(S_0) . \quad (10)$$

190 In the following, the subscript V is dropped for simplicity, and all TFR values are in units of
 191 volume per time. To avoid confusion when referring to a strong (more negative) TFR , the sign for
 192 the TFR caused by eddy mixing will be reversed in all the plots.

193 With this setup we purposely neglect all other processes that influence the SSS in the real ocean
 194 like the surface forcing and all vertical processes, e.g. subduction, entrainment and diapycnal

195 mixing. The robust nature of this diagnostic, which relies just on the area within a contour and
 196 isolation of the mixing effect of the observed velocities enables the study of temporal variability
 197 in eddy mixing. The downside of this approach clearly is the integral character of the results. It
 198 is not possible to diagnose local extrema in fluxes. It is well suited for the purpose of this study,
 199 since the main interest lies in the role of lateral eddy mixing to the formation and maintenance of
 200 the large scale SSS-maxima.

201 *a. Surface forcing compensation*

202 Transformation rates by eddy mixing are compared to the volume transformation rates by surface
 203 forcing in salinity coordinates (using equations 3 and 6):

$$TFR_{EP,V}(S_0, t) = \frac{\partial}{\partial S_0} \iint_{(S \geq S_0)} S(E - P) dA \quad (11)$$

204 To analyze the importance of eddy mixing to the budget, we compare the ratio of *TFR* due to eddy
 205 mixing with the *TFR* due to surface forcing. We call this ratio the surface forcing compensation
 206 (SFC):

$$SFC = - \frac{\overline{TFR_{Eddy}(S_0, t)}}{\overline{TFR_{EP}(S_0, t)}} \quad (12)$$

207 *b. Effective diffusivities*

208 It is worth dissecting variability of the *TFR* into contributions from variability in the stirring
 209 (velocity fluctuations) and variability in the background salinity field, which includes changes in
 210 local gradients as well as a changing position of the reference isohaline. To isolate the effect of
 211 the velocity fluctuations, we calculate the effective diffusivity. This method uses the same water
 212 mass frame of reference as the *TFR* and is thus directly comparable to the other results.

213 The effective diffusivity is a diagnostic developed by (Nakamura 1996) to measure the diffusive
 214 transport across an instantaneous tracer contour. It represents the net mixing integrated along the

215 tracer contour (salinity contour in our case). The effective diffusivity for a tracer q can be written
216 as

$$K_{eff}(q) = \kappa \frac{L_e^2(q)}{L_{min}^2} \quad (13)$$

217 where κ is the molecular (or grid-scale) diffusivity, L_e is the “equivalent length” of an instanta-
218 neous tracer contour, and L_{min} is the minimum possible length that contour can achieve under a
219 conservative rearrangement of the tracer field (Marshall et al. 2006). L_e can be calculated from
220 the instantaneous tracer field. Stirring by mesoscale turbulence leads to highly filamented tracer
221 contours and causes L_e to be many times greater than L_{min} , leading to enhanced mixing. The
222 ratio L_e^2/L_{min}^2 quantifies the relative enhancement of molecular / grid-scale diffusivity due to this
223 stirring. Although K_{eff} formally depends on κ , it was shown by Marshall et al. (2006) that this
224 dependence drops out in the high-Peclet-number regime because L_e^2 also depends inversely on κ .

225 Following Nakamura (1996), the equivalent length of any tracer contour q can be calculated as:

$$L_e^2(q) = \frac{\frac{d}{dA} \int |\nabla q|^2 dA}{\left(\frac{\partial q}{\partial A}\right)^2} \quad (14)$$

226 As described therein this value can be evaluated at any tracer time step and is then mapped back
227 to a ‘reference position’, in this case the tracer contour position in the smooth initial field of each
228 experiment. The minimal length of the contour L_{min}^2 is simply the L_e^2 value corresponding with the
229 initial condition of each experiment, before stirring has caused any filamentation of the contour.

230 Even though this diagnostic has been mostly used in scenarios with a high degree of uniformity
231 in the zonal direction like the Southern Ocean (Abernathay et al. 2010) and the central part of
232 the Pacific (Abernathay and Marshall 2013), it can be applied to any tracer field. An example of
233 this application can be found in Lee et al. (2009), who studied the effective diffusivity of a tracer
234 patch released in the subtropical gyre. In the case of the SSS-max, the salinity contour values map
235 geographically to the distance from the center of the maximum.

236 The effective diffusivity is not defined for a vanishing background gradient. To avoid the oc-
237 currence of weak tracer gradients our initial conditions are reset in regular intervals as described
238 below.

239 *c. Data*

240 We use absolute geostrophic velocities from the AVISO DUACS2014 (1993-2014) alti-
241 metry product, produced by Ssalto/Duacs and distributed by Aviso, with support from Cnes
242 (<http://www.aviso.altimetry.fr/duacs/>). The data is subset in weekly fields and has a native spa-
243 tial resolution of 1/4 degree. We assume that the velocity fluctuation of the largest most energetic
244 eddies are captured by this data. The long standing AVISO record represents our current best es-
245 timate of the surface eddy field. Since there is no similarly long, global observational record of
246 higher resolution we are not able to investigate how unresolved velocity structures influence the
247 results. Such a comparison will be left to future studies. The geostrophic velocities do not include
248 the Ekman velocities at the surface, but as Rypina et al. (2012) show, these have little influence on
249 the mixing characteristics at the surface. Climatological SSS fields as well as mixed layer depth
250 are taken from the MIMOC-Argo climatology (Schmidtko et al. 2013). The data are given as
251 climatological months with a spatial resolution of 1/2 degree. Additionally annual SSS fields are
252 used from ECCO-MIT v4 r2 ocean state estimate (Forget et al. 2015) and the ADPRC gridded
253 Argo product (<http://apdrc.soest.hawaii.edu/projects/Argo/data/gridded/>).

254 E data is taken from the OAFlux (Yu et al. 2008) monthly mean product and P from the Global
255 Precipitation Climatology Project (GPCP) (Huffman et al. 2010), both of which have a spatial
256 resolution of 1 degree. The fields are averaged into climatological monthly means and interpolated
257 on the MIMOC grid for analysis.

258 *d. Model setup*

259 We conduct a suite of experiments by stirring initial SSS fields with observed velocities. From
260 these experiments, we diagnose the transformation rate by eddy mixing and surface forcing as well
261 as the effective diffusivity.

262 The basis for this study are numerical experiments run in the MITgcm (Marshall et al. 1997) fol-
263 lowing the setup of Abernathey and Marshall (2013). The model output is calculated in 900 second
264 intervals and tracer snapshots are output every 7 days. Initial SSS fields are passively advected by
265 7-day snapshots of two-dimensional AVISO absolute geostrophic velocities after both have been
266 interpolated onto the 1/10 deg. model grid. The velocities need to be slightly corrected in order
267 to be non-divergent, using the procedure described in Abernathey and Marshall (2013) Appendix
268 A. The only difference from that study is that here we used the newer DUACS 2014 product from
269 AVISO. Tracer transport across isolines can only be achieved via the model’s prescribed grid-scale
270 diffusivity κ (the schematic in Figure 1 illustrates the process). However as discussed in detail in
271 Abernathey and Marshall (2013) and references therein, the width of tracer filaments (and thereby
272 L_e^2) is also dependent on κ , in such a way that the effective diffusivity is largely independent of this
273 value. This makes the results robust in the sense that they are not governed by an internal “tuning”
274 parameter of the model but instead depend almost completely on the velocity input, which is de-
275 rived from observations. The small scale diffusivity for these model experiments was diagnosed
276 as $\kappa = 63m^2/s$ (Table B1, Abernathey and Marshall 2013).

277 In addition to calculating long-term averages of TFR_{Eddy} and K_{eff} , we expanded the method
278 with the explicit goal of resolving temporal fluctuations in eddy mixing. Due to the lack of a
279 restoring mechanism for the tracer, over long time scales the tracer field will increasingly ho-
280 mogenize and large-scale features might be deformed and shifted. In a homogenized tracer field

no mesoscale velocity can produce a tracer fluctuation and the diagnostics presented here become meaningless. The advection and deformation of large-scale features will impact a useful remapping of the results to the initial conditions. This prompts us to reset the tracer fields in regular intervals, or results could not be interpreted anymore using the initial position of the SSS-maxima. This methodology is well suited to examine the SSS-maxima in the subtropical gyres, since mean advection is relatively low and the main features are not advected out of their original position quickly. Two tracers are simulated in parallel and reset at different phase and the results are averaged to eliminate any residual drift in the diagnostics and maintain the background field “quasi- constant”. We obtained an uncertainty associated with the reset period by comparing certain ranges. All results that are discussed as significant exceed this uncertainty, and are as such assumed to be robust features of the input fields derived from observations. For further details see Appendix.

293 *e. Initial conditions*

Each setup as described above will result in time series of TFR and K_{eff} for each basin, describing the influence of a changing velocity field, which evolves with time but is the same in each experiment. The results might depend of the initial condition, which determines the position and hence exposure of the reference isohaline to possibly different features of the velocity field. To investigate the eddy mixing sensitivity to changes in the initial conditions we evaluate a suite of experiments with varying tracer initial conditions, all of which are averaged SSS fields. These are reset in an identical manner as described above , keeping each of the different initial conditions “quasi-constant”. Nothing but the initial condition is changed between the various experiments. In the following each experiment is denoted by a suffix indicating the initial conditions used as outlined in Tab. 1.

304 Comparison between the different initial condition experiments then gives an indication of the
305 sensitivity of the results to the variable background fields. None of these experiments will give a
306 realistic representation of the actual variations in eddy mixing which are likely to depend on both
307 variable velocities and SSS fields.

308 Consider a strong stirring anomaly that only occurs during a time X. One of the SSS-max fea-
309 tures could 'move' into that particular region during time Y. This would result in a strong variation
310 of the diffusivity and TFR in the experiments with the initial conditions close to time Y. This how-
311 ever could be irrelevant for the 'actual' SSS-max when time X is not equal to time Y, or it could
312 even emphasize the variability when they are equal. To get a crude estimate of such a combined
313 variability we introduce the "combined" experiments. These are not separate experiments, but in-
314 stead combine the results of the existing experiments according to the matching initial conditions.

315 This still does not provide a fully resolved time series for each basin, but it provides a guide for
316 interpreting the importance of variability in diffusivity and transformation rate and exclude com-
317 pletely improbable scenarios that can arise due to the combination of the full variable velocity
318 record with averaged and non-evolving initial conditions. Using these estimates we can investi-
319 gate situations where the spread between experiments is large and whether any detected variability
320 could be significant for the real world SSS-max

321 The procedure is explained in detail in the Appendix and shown schematically in Figure A2.

322 To summarize the main diagnostics used in this paper before we discuss the results:

- 323 • Effective Diffusivity: The cross isohaline eddy diffusivity, relevant for water mass transfor-
324 mation. A measure of the stirring strength of the velocity field on the boundary of the volume,
325 not dependent on the background gradient.

- 326 • TFR : A measure of the integrated diffusive flux into the volume bounded by an isohaline.

327 Compared to the effective diffusivity TFR incorporates both the velocity statistics and the
328 background gradient.

- 329 • SFC: The comparison of the lateral diffusive flux into the volume vs. the surface forcing
330 integrated over the corresponding sea surface. This gives an indication of how important
331 surface eddy mixing is for the volume budget.

332 3. Results

333 The mean salinity differs significantly between the global ocean basins. In order to compare the
334 saltiest regions, we use the reference salinities S_{ref} from (Gordon et al. 2015). Each basin is then
335 analyzed in regional boxes to ensure the values represent only the SSS-max region and not other
336 areas with identical salinities. See Figure 2 for the position of the reference salinities as well as
337 the regional boxes used.

338 a. Mean

339 The results for the mean SSS fields can be seen in Figure 3, with each of the diagnostics plotted
340 against the bounding salinity contour with the regional reference salinity subtracted. The purpose
341 of showing the full salinity domain is to demonstrate that, within the highest salinities of each
342 basin, the results are relatively constant and not strongly dependent on the choice of the reference
343 salinity. Hence for all further analysis we show the values on the basin specific reference isohaline
344 S_{ref} only (indicated by the horizontal line in Figure 3).

345 Note that the lower values represent isohalines further outward from the SSS-max. Thus they
346 might not be contained within the regional boxes. This will violate the previously outlined equa-
347 tions, by introducing a non zero lateral boundary flux. As discussed later in the Appendix, the

348 low lateral gradient in the Southern Indian (SI) presents a problem with regard to this constraint.

349 Outer salinities in the SI should be regarded as unreliable. We confirmed that for all experiments

350 the actual reference isohaline is well contained in the regional domains (see Appendix).

351 Figure 3 shows the $TFR_{Eddy,mean}$ is highest in the SI and North Pacific (NP) with mean values

352 of about 3.4/3.5Sv. The other basins show lower TFR with the North Atlantic (NA) at about 2

353 Sv, followed by the South Atlantic (SA) with about 1.5 Sv and the South Pacific (SP) with 1.2

354 Sv. The difference between the NP/SI and NA/SA/SP might reflect the larger area within salinity

355 contours due to the weaker lateral salinity gradient and do not necessarily indicate a higher relative

356 contribution to the budget by eddy mixing. The SFC (Figure 3b) illustrates this by showing what

357 percentage of the TFR_{EP} is compensated by $TFR_{Eddy,mean}$. Here the SI still has the highest value

358 (25%) while the NP is found well in the spread of the other basins. The standout basin in terms

359 of TFR and SFC seems to be the SP that shows the lowest SFC at $< 10\%$ for salinities $< S_{ref}$

360 throughout most of the salinity space. The NA which in terms of salinity processes has received

361 the majority of the attention in the science community during recent years has a SFC of around

362 20%.

363 Regional differences also emerge in the diffusivities (Figure 3c). The SP again shows the lowest

364 values compared to the other regions. But the basin ranking in SFC is not mirrored in all the K_{eff}

365 values. Most notably, the SI has weak diffusivity values while the transformation rate is highest.

366 Alignment of high local diffusivities with high gradients that dominate the overall TFR , and in

367 turn the SFC , are necessary to explain this behavior. This illustrates that localized structures can

368 be decisive for the total diffusive flux out of the SSS-max. The effects of these structures for the

369 mean quantities is captured with the methods used here, but it is not possible to locate these “hot

370 spots” in space with our method.

³⁷¹ Any localized covariance between gradient and diffusivity is important for understanding tem-
³⁷² poral variability in eddy mixing. Our observation driven model studies are therefore well posed to
³⁷³ investigate temporal variability in eddy mixing by representing the interrelated variability of the
³⁷⁴ SSS and eddy fields in both time and space.

³⁷⁵ *b. Comparison to existing studies*

³⁷⁶ To our knowledge the closest studies using a comparable control volume (isohaline coordinates)
³⁷⁷ are Bryan and Bachman (2014) (North Atlantic only) and Johnson et al. (2016) (global). Both
³⁷⁸ studies use the same methodology and model setup. Another study by Schmitt and Blair (2015)
³⁷⁹ applies diffusivity estimates to a climatology in a similar framework and finds similar results as
³⁸⁰ Bryan and Bachman (2014). They investigate the full volume bounded by the isohaline, including
³⁸¹ the subsurface below the mixed layer. There are some caveats to the comparison as outlined below,
³⁸² but as we conclude, the most striking regional characteristics seem robust when compared to our
³⁸³ results.

³⁸⁴ The comparison between the three studies above might be complicated by several issues. The
³⁸⁵ model studies show large biases in their surface salinity fields, which changes the mean position
³⁸⁶ of the outcrop area. Hence even when we present our results in the exact reference salinities of
³⁸⁷ their study, the bounded area can vary significantly. This could not only affect the water mass
³⁸⁸ transformation by eddy mixing but also the appropriate surface forcing term. Bryan and Bachman
³⁸⁹ (2014) show a comparison of the forcing term and the water mass transformation rate due to
³⁹⁰ surface fluxes, where the model term deviates significantly from estimates using climatological
³⁹¹ data sets (their Figure 11).

392 In order to compare our results with these previous studies, most of which evaluate the salinity
393 budget, we additionally calculated the SFC for the salinity budget. By integrating the right hand
394 side of Equation 9 and 11 in salinity space and dividing them similar to Equation 12.

395 Results are shown in Table 2 as SFC_S . Furthermore we evaluated all results on the reference
396 salinities from Johnson et al. (2016) (Table 2; gray columns). For each basin except the SI, the
397 difference in the various SFC values is 5% or smaller, a minor difference considering the spread
398 in regional results from previous studies (e.g. 10-50% SFC in the NA). We will discuss possible
399 reason for the wide range of results below.

400 Some similarities emerge: The SP SSS-max has the weakest eddy mixing contribution both for
401 the mixed layer and the full isohaline volume. Our results using the SFC based on the volume bud-
402 get as well as the full depth results from Johnson et al. (2016) suggest that the largest contribution
403 by eddy mixing is found in the SI. Results for alternative reference salinities might be biased since
404 the area within the isohaline could be leaving the regional boundary in our study (see Appendix).

405 The remaining basins differ in their ranking depending on the metric used. It should not come
406 as a surprise that not all basins compare well in both studies, as the comparison is between eddy
407 mixing estimates for the mixed layer only versus the full depth isohaline volume. Assuming the
408 results are indeed comparable, despite the aforementioned reasons, one can estimate a crude ratio
409 of SFC between the mixed layer and the interior by comparing the SFC values to each other
410 (Table 2; last row). The ratio varies from 22% up to 37%. Given the small surface area of the
411 lateral mixed layer boundary compared to the surface of the subsurface isohaline volume this might
412 indicate a significant depth dependency of the lateral eddy mixing - strong in the mixed layer and
413 comparably weak in the interior. Further research has to show to what degree these studies are
414 actually comparable and if these findings can be confirmed from independent estimates.

415 Besides the choice of control volume, the actual quantification method for F_{Eddy} could matter
416 for the resulting SFC . Gordon and Giulivi (2014) proposed the idea of eddy fluxes as a significant
417 contribution to the salinity/freshwater budget in the North Atlantic SSS-max region. They estimate
418 the covariance term from SODA reanalysis data by defining the prime terms as the deviation from
419 the zonal average over a box that is approximately 25 degrees wide. This is about 50 times the
420 range of the first Rossby Radius in this area (about 50km (Chelton et al. 1998)), possibly including
421 large scale circulation features in the prime terms. This potentially biases the contribution of eddy
422 mixing by adding some of the long term advective variability. That would explain why this study
423 concludes the highest SFC in the mixed layer of the North Atlantic at around 50%. Our results
424 agree reasonably well with Busecke et al. (2014), who estimated 10%-30% SFC in the NA mixed
425 layer based on the distribution of local divergence of eddy diffusion by using a constant scalar
426 eddy diffusivity and a typical SSS curvature found in a similar box as Gordon and Giulivi (2014).
427 The choice of a “typical” SSS-curvature might effectively mitigate some of the variability caused
428 by the moving SSS-max combined with a fixed control volume.

429 *c. Seasonal variability*

430 We find that temporal variability exists in the TFR as well as K_{eff} on various time scales.
431 We focus on the seasonal and interannual signal. In agreement with Bryan and Bachman (2014)
432 and Johnson et al. (2016), this variability is small compared to the other terms in the volume
433 budget (not shown), namely surface forcing and vertical diffusion. Since these two effects are
434 largely compensating, the eddy mixing can still play an important role for the tendency term in
435 the volume budget of the SSS-maxima. Indeed variations in interannual $TFR_{Eddy,mean}$ are of
436 comparable magnitude as the TFR calculated from the actual change in area from observations
437 (using the same fixed MLD, not shown).

438 Before we present the results, we begin with a discussion of mechanisms that can cause a tem-
439 poral variability in the TFR. We will assume that the diffusive flux across the contour is expressed
440 as the product of a mean cross-contour diffusivity K_{eff} and the salinity gradient on the contour
441 $\nabla_l S$ (by definition perpendicular to the contour). As outlined above K_{eff} itself is independent of
442 the background gradient, since it only measures the enhancement of a spatial gradient (which has
443 to be non-zero) by the stirring action of a given velocity field. The resulting flux will scale with
444 both the cross-contour diffusivity as well as the cross contour gradient. Since K_{eff} is the result
445 of the velocities acting on the background fields, and the velocities can vary both in space and
446 time, there are three principal mechanism that could cause temporal variability in TFR. In each
447 basin there is likely a contribution by each of these mechanisms but in the following list we lay out
448 how each mechanism would affect the results in isolation in order to facilitate the identification of
449 the dominant process within the results that follow:

- 450 1. Change of K_{eff} due to temporal variability in the velocity field. Assume the velocity field
451 would have spatially homogeneous stirring characteristics which vary with time. All experi-
452 ment would show coherent variability in both TFR and K_{eff} , since for each experiment the
453 position of the cross-contour gradient is constrained by the reset procedure, hence the diffu-
454 sivity would control the time evolution of the TFR .
- 455 2. Change of K_{eff} due to changes in the position of the contour in a field of spatially variable
456 stirring. Opposite to above now assume a temporally constant stirring action of the velocity
457 field which varies in space instead. All experiments would show constant TFR and K_{eff} ,
458 since for a constrained contour in a single experiment the stirring action resulting in K_{eff}
459 as well as the cross contour gradient would remain 'quasi-constant'. The position of the

reference contour varies between each experiment, potentially exposed to other parts of the velocity field. This would cause a spread between experiments in both TFR and K_{eff} .

3. Change in salinity gradient $\nabla_l S$ on the contour. As explained above, single experiments would show no variability in either TFR or K_{eff} , since the gradient is constrained by the reset. Experiments would show constant TFR and K_{eff} as in 2, however the spread between experiments only affects TFR . Contrary to 2 the K_{eff} would remain constant between experiments, since the stirring characteristics and the contour position are identical and K_{eff} is independent from the background gradient (see section 2).

These idealized mechanisms are assuming that any change in gradient or diffusivity along the contour is represented well by a mean value. If strong heterogeneity along the contour occurs the TFR and K_{eff} values shown here within a single experiment could show low temporal coherency, especially when the “along-contour” anomalies of diffusivity and gradient covary.

The left column in Figure 4 shows the seasonal cycle for each experiment, separated into ocean basins. The seasonal cycle extracted from the experiments with monthly (gray lines), mean (blue line) initial conditions and the combined (black) experiment are shown. Regional differences in the seasonal cycle are evident. The combined seasonal cycle in the SI and SP is very small or not truly an annual harmonic. In the NA, SA and NP the combined seasonal cycle is of significant size compared to the mean and is shaped close to an annual harmonic with the highest values during the spring of the respective hemisphere. The SI and SP show relatively weak seasonal cycles in $K_{eff,mean}$ (red line), that cannot be related to the TFR_{mean} in a straightforward manner, suggesting increased importance of the local interplay of diffusivities and gradients or simply a non-significant seasonal signal.

482 We want to focus on the NP and NA in particular as they seem to display two regionally different
483 origins of the combined seasonality related to the idealized scenarios from above. In the NA every
484 experiment with monthly initial condition is exhibiting a very similar seasonal cycle in terms of
485 timing and amplitude. When comparing the K_{eff} values for the NA (Figure 5a) the variability
486 is very coherent and larger than the offset between the single experiments. This suggests a local
487 change in diffusivities (mechanism 1 from above) as the leading cause of variability in the NA. The
488 time lag of about a month between $K_{eff,mean}$ and TFR_{mean} in the NA (Figure 4a) is an interesting
489 result in itself, which is robust for all experiments (not shown). We interpret the lag as the time
490 between the fast creation of lateral tracer gradient variance (stirring, reflected in K_{eff} which is then
491 slowly digested by small scale diffusion acting on this gradient variance). This yet again illustrates
492 the complex nature of the eddy mixing and the problems which may arise when eddy mixing is
493 diagnosed from methods involving matching of vastly different data sets. Due to the less coherent
494 signals in other basins it is unclear if the length of this lag is the same in every basin.

495 In the NP the TFR of each experiment seems to be rather constant with a larger offset in between
496 experiments. The K_{eff} values in Figure 5a show a similar offset between experiments as the NA,
497 but in the case of the NP it is not small compared to the annual cycle. Hence it seems likely that
498 a change in diffusivity due to the changing position is responsible for the variability in TFR . This
499 is plausible if we consider the variable position of the NP S_{ref} contour and its vicinity to strong
500 gradients in surface diffusivities (Figure 2). We cannot rule out a change in local gradient on the
501 contour as a contribution. It is clear however that in the NP the initial fields of SSS are more
502 important for the variability in eddy mixing than the velocity field, contrary to the NA.

503 The SA exhibits the largest spread in K_{eff} between experiments. We suggest that this is caused
504 by its unique position in the western boundary current. The SA SSS-max is exposed to strong
505 advection, possibly moving in and out of areas of spatially heterogeneous diffusivities. This does

506 not result in a clear seasonal cycle as in the NA and NP and it is left for further studies to determine
507 whether this large variability remains robust when other processes (as mentioned in the method
508 section) are invoked. We will now apply the same analysis to the interannual signals to investigate
509 if we find evidence for local changes of diffusivities on time scales longer than a year.

510 *d. Interannual variability*

511 Figure 4 (right column) and Figure 5 (right) show interannual variability of K_{eff} and TFR .

512 Similar to the seasonal plots, the gray lines in Figure 4, right column, mark each experiment
513 with annual averaged initial conditions, while the $TFR_{annual,combined}$ is shown in black. The com-
514 bined experiment should be viewed as a check whether various initial conditions can change or
515 compensate the variability imposed by the velocity field.

516 The character of the longer-term variations is quite different between basins. The NA TFR
517 increases till ca. 2006 and then decreases in a similar fashion. This is consistent with the combined
518 ECCO experiment but the combined ARGO experiment shows an offset which suggests the TFR
519 to stay high in the later part of the record. The SA shows several shorter fluctuations while the
520 longer term seems to be quite steady.

521 The NP shows an increase in K_{eff} and TFR around 1998 in several experiments. For the SSS-
522 max this seems to be rather irrelevant, since the combined experiment does not capture it. Towards
523 the end of the record the TFR seems to decrease slightly. Similar to the seasonal cycle, the NP
524 shows the largest spread between experiments compared to all other basins, again indicating the
525 possible larger sensitivity to changes in SSS fields compared to the other basins.

526 The SP shows a strong maximum in $TFR_{annual}/K_{eff,annual}$ in 1998. When the combined exper-
527 iment is considered, the amplitude is lessened somewhat but the peak remains the largest interan-
528 nual anomaly in all ocean basins.

529 The SI again shows very little variability, similarly to the seasonal cycle.
530 The comparison between the combined experiments from ARGO and ECCO suggests that re-
531 sults in the NA and to a lesser degree in the SP are sensitive to the source of initial conditions. In
532 the SA,NP and SI the records diverge only slightly. Especially for the earlier years of the ARGO
533 record the mismatch might be caused by limited float coverage.

534 It is worth noting that in the SP (and in many experiments for the NP) the variability in eddy
535 mixing seems to be roughly coincident with the strong El Niño of 1997-1998.

536 This indicates that large scale environmental processes might be linked to time variable mixing
537 relevant for the subtropical SSS-maxima. The tight distribution of $K_{eff,annual}$ values for the NA
538 and SP suggest that these changes are mainly caused by local changes in diffusivity which appear
539 very coherent in space, affecting most experiments. Even in the NP the high number of experi-
540 ments showing a peak around 1998 contribute to this idea. The SSS-max might not be impacted
541 by the anomalous velocities, due to an anomalous contour position, but it indicates that diffusivity
542 changes might be happening adjacent to the SSS-max.

543 These results suggest a link between large scale climate forcing and the eddy mixing in the NA
544 and SP SSS-max via locally changing diffusivities (mechanism 1 from above).

545 The SA and NP show considerable spread between the K_{eff} values. Similar to the seasonal
546 interpretation, we conclude that the changing position of the reference isohaline is the dominant
547 driver for the variability in the NP and SA. Both of these basins show larger lateral gradients in
548 surface diffusivities (Abernathay and Marshall 2013), qualitatively confirming the potential for
549 high variability in diffusivites by changing the position of the reference isohaline.

550 The SI shows little spread in K_{eff} and little variability in the single experiments. The variability
551 in TFR is also low compared to the other basins. This is particularly interesting since it has
552 arguably the largest contribution of eddy mixing to the budget, while having both a small mean

553 diffusivity and by far the least variability. Local “hot spots” for the eddy mixing (locations where
554 diffusivity and gradient line up locally to dominate the overall TFR) could explain the discrepancy
555 between the high integrated diffusive flux and the low averaged diffusivity.

556 The following list summarizes the regional “character” (lending from Gordon et al. (2015)) of
557 each basin with respect to the eddy mixing in the surface layer:

558 • The SP has by far the lowest SFC of all the basins. This is likely due to its unique separation
559 from the western boundary current. The Southern Inter-tropical Convergence Zone shifts the
560 SSS-max far into the eastern part of the basin, prohibiting access to the energetic western
561 region of the basin. The seasonal cycle is very irregular although the amplitude is relatively
562 higher than in the SI in agreement with Gordon et al. (2015) Figure 3. The interannual record
563 shows the strongest signal of all basins with a strong pulse of elevated TFR and K_{eff} around
564 1998, which is proposed to be related to larger scale climate variability modulating local
565 diffusivities with time.

566 • The SI is the strongest basin in terms of SFC and TFR but interestingly very low K_{eff} and low
567 temporal variability in eddy mixing, possibly influenced by its unique poleward position in a
568 predominantly zonal mean flow, stabilizing seasonal gradients and possibly suppressing the
569 eddy diffusivities in a region relatively high in EKE (e.g. Klocker and Abernathey (2014)).

570 • The SA has a similar SFC to the NP and NA and shows a less coherent seasonal cycle in TFR
571 that is similar in magnitude and timing (with a 6 month shift accounting for the hemispheric
572 difference) to the NP and NA. It seems that it represents somewhat of a mixed case in terms
573 of the responsible mechanism (local diffusivity changes vs. monthly SSS fields).

574 • The NA seems to be largely dominated by local changes in diffusivities both for the seasonal
575 and interannual variability. What exactly renders this mechanism so dominant in the NA

576 is subject to speculation: It might be related to the high lateral salinity gradient (inhibiting
577 strong lateral movement of the reference isohaline) or the relatively low lateral gradient in
578 surface diffusivities which further reduce the influence of a changing isohaline position to the
579 effective diffusivity.

- 580 • The NP variability in eddy mixing is strongly dependent on the SSS fields. Both the seasonal
581 cycle as well as interannual variability are shown to be strongly influenced by the position of
582 the reference isohaline, supported by conditions of low lateral SSS gradient and high surface
583 diffusivity gradient. The interannual record shows some indications of a long term change
584 which might be caused by local changes in the diffusivites similar to the SP and NA.

585 4. Conclusions

586 a. Relevance for the SSS-maxima in the global ocean

587 Using diagnostics for eddy diffusivity and integrated diffusive flux in a water mass framework,
588 we documented marked regional differences in the strength, variability and the responsible mech-
589 anisms for eddy mixing in the SSS-maxima.

590 The temporal variability of the eddy mixing is a result of regionally differing mechanisms, dom-
591 inated by variability in either the velocity field or the surface salinity field: On the one hand local
592 changes of the eddy field resulting in local diffusivity changes and on the other hand changes in
593 the position of the SSS-maximum in a spatially varying field of surface diffusivities.

594 The results presented here support the notion of each of the SSS-maxima having his own unique
595 character in eddy mixing, in agreement with the results from Gordon et al. (2015) for the mean
596 position and strength of the seasonal cycle.

597 We argue that temporal variability of eddy mixing and diffusivities has to be taken into account
598 when constructing salinity budgets in the SSS-max regions. Furthermore the application of results
599 from one SSS-max region (e.g. the well studied NA) to other basins might not be possible. Es-
600 pecially when considering a changing climate, which might influence the mechanisms responsible
601 for temporal variability differently.

602 *b. Implications for the global water cycle*

603 Regional differences in eddy mixing could have implications for the diagnosis of water cycle
604 changes using the SSS on long time scales. If the common conception of an intensifying water
605 cycle in the future — “saltier regions get saltier and fresh regions become fresher” (Held and Soden
606 2006) — holds true, these changes might influence the eddy mixing in each basin differently. For
607 instance, the NP shows the highest sensitivity to changes in the surface salinity. Presumably
608 higher eddy mixing would ensue following the intensification of the lateral salinity gradient by an
609 intensified hydrological cycle, and one could imagine a negative feedback. Of course this would
610 only be valid if the eddy diffusivities remain constant, an assumption that cannot be validated for
611 the relevant time scales (more than 50 yrs (Durack and Wijffels 2010)) at this point. It seems
612 indeed that the observed decadal pattern intensification in SSS are especially weak/inconsistent
613 in the NP, both for strongly forced model runs as well as historic observations ((Durack 2015),
614 their Figure 7 A/D). This would be in line with the argument presented above. Further research
615 is needed to investigate this mechanism and its potential importance for the imprint of a changing
616 hydrological cycle on the SSS.

617 *c. Beyond the surface salinity*

618 This study suggests basin scale changes of the local surface diffusivities, potentially affecting
619 areas much broader than the SSS-max. In the case of the South and North Pacific these changes
620 seem connected to large scale climate fluctuations related to ENSO, possibly forming an important
621 climate feedback. To our knowledge such a connection has not been documented using an obser-
622 vationally driven method and could be of relevance to the larger oceanographic and climate science
623 community. A data set of monthly surface diffusivities combining methods from Abernathey and
624 Marshall (2013) and this study will be helpful in identifying locations where eddy diffusivities
625 respond coherently to the large scale environment. Such a data set is in preparation and will be
626 published in a separate manuscript.

627 *Acknowledgments.* We are grateful for the detailed comments from two anonymous reviewers,
628 which greatly improved the manuscript. We also thank Sjoerd Groeskamp, Sloan Coats, Claudia
629 Giulivi and Søren Thomsen for comments on the initial draft. Julius Busecke’s research was sup-
630 ported by NASA award NNX14AP29H. Ryan P. Abernathey acknowledges support from NASA
631 award NNX14AI46G. Arnold L. Gordon’s research is supported by NASA grant NNX14AI90G
632 to Columbia University. Lamont-Doherty Earth Observatory contribution number XXXX.

633 APPENDIX

634 *a. Reset procedure*

635 Due to the nature of the presented experiments, which do not simulate key processes like surface
636 forcing and all vertical processes a steady state will never be reached in the TFR/K_{eff} . The mixing
637 will eventually just destroy all local maxima and completely homogenize the surface fields. In
638 order to maintain a realistic “quasi-constant” background SSS field the tracer fields have to be

639 reset in regular intervals. Each reset to the smooth initial conditions causes a distinct spike in
640 both TFR and K_{eff} , which represents the adjustment phase in which increased variance is created
641 by stirring the smooth initial conditions until the small scale diffusion limits the variance and the
642 change in TFR and K_{eff} represents the temporal changes in eddy stirring. The aforementioned
643 adjustment phase is unrealistic and has to be removed (we cut the first 2 months in our experiments,
644 leaving a gap in the data record. We compute two different tracer outputs that are reset at shifted
645 intervals and then averaged, to create a continuous time series of TFR and K_{eff} for each salinity
646 S_0 . Shifting them exactly half of the reset period also ensures that any residual drift from the reset
647 would be averaged out. Several considerations are influencing the choice of reset period:

- 648 • The missing data might still slightly bias the results at the time of reset. It is vital to choose
649 an odd number of months as the interval length, to ensure that the possible effect of the reset
650 is occurring at different months of the year each time, which should be averaged out when
651 analyzing the seasonal cycle.
- 652 • The mean position and area of the SSS-max features have to remain within a realistic range,
653 which limits the maximal length of the reset interval to 9-11 months. After that for instance
654 the NA SSS-max get slowly advected into the equatorial current system and the velocity
655 fluctuations acting on the reference isohaline are not representative of the subtropics anymore.
- 656 • The reset interval has to be chosen so that the reference salinity does not get eroded too far,
657 which specifically in the SI is a problem in reset periods over 9 months
- 658 • Since the adjustment phase removes 2 months from the record, the reset period is chosen as
659 long as possibly allowed by the above criteria, to ensure a maximum of data points are derived
660 from both tracer records.

661 We hence decided on a reset period of 9 months, with the second tracer field initiated again after
662 4.5 months and then reset in 9 months intervals like the first.

663 *b. Error due to reset procedure*

664 To estimate the influence of the chosen reset interval we conducted several quality control (QC)
665 experiments with varying reset intervals (7/9/11/13 months), all reset to the mean SSS initial con-
666 ditions. Results for $TFR_{mean}/K_{eff,mean}$ are calculated identically to the presented data for mean,
667 seasonal and interannual. We estimate the RMSE as:

$$RMSE = \sqrt{\langle\langle x \rangle_{(ex)} - x_{t,ex} \rangle_{(t,ex)}} \quad (A1)$$

668 Where $\langle . \rangle_{(ex)}$ is the average over all QC experiments without averaging in time and $\langle . \rangle_{(t,ex)}$ is the
669 average over time and experiments. Figure A1 shows the estimated error split into the various
670 temporal estimates. Results discussed as significant exceed these error estimates and are assumed
671 not to be strongly dependent on the reset procedure .

672 *c. Combined experiment*

673 In order to evaluate the effect of the interplay between temporally evolving velocities and SSS
674 fields we created several “combined” experiments. As stated above they are not separate model
675 experiments, but instead combinations of the single experiments, aiming to give the most realistic
676 representation of the TFR for a climatological season or interannual variability. We split the ex-
677 isting experiments into chunks and stitch them together in order of their initial conditions. For the
678 ’annual combined’ from January 2000 until December 2000 the values are taken from the ’ECCO
679 2000’ experiment (see Table 1) and from January 2001 until December 2001 the values from the
680 ’ECCO 2001’ experiment (see Table 1) are inserted. This is repeated for all annual experiments.
681 We present two ’annual combined’ records to cover the whole time frame of the altimetry record.

682 From 1993-2011 we use annually averaged surface fields from ECCO as intial conditions and from
683 2006 to 2014 we use Argo data (details in Tab. 1).

684 The 'monthly combined' experiment is created by substituting each month in the record with
685 data from the experiment with corresponding climatological initial conditions (see Figure A2).
686 Note that these are climatological monthly initial conditions, meaning the initial conditions are the
687 same for each e.g. January. The velocities however vary interannually as in all other experiments.

688 *d. Boundary violation*

689 The water mass framework is well suited for the study of SSS-maxima due to their appearance as
690 local maxima in the SSS fields. One however has to define regional domains in order to not lump
691 all maxima together globally, making the interpretation of local differences impossible. Depending
692 on the basin the definition of this local domain can be complicated as one has to take good care
693 that the isolines of interest neither leave the box at any time nor other features enter the domain.
694 Our domains are chosen to guarantee both of these aspects for the reference salinity. Due to the
695 regional setup this can mean that even isolines as little away as 0.2 PSU violate this criterion. This
696 is especially critical in basins with low lateral SSS gradients and secondary local maxima in SSS
697 like the SI and NP. In fact in the SI we were not able to completely keep the reference isohaline
698 in the box without making the box unreasonably large, reaching into the SA and SP. Hence we
699 decided to allow a possible but likely small leakage of the reference isohaline on the South coast
700 of Australia. Values at isohalines larger than the reference salinity are not affected by the boundary
701 violation but might be biased due to the fact that the highest salinity values will simply disappear
702 over the reset time, as they diffuse outwards. Thus we urge the reader to interpret the values only
703 on the reference salinity, for which extensive testing has excluded above issues.

704 **References**

- 705 Abernathey, R., J. Marshall, M. Mazloff, E. Shuckburgh, R. Abernathey, M. Mazloff, and
706 E. Shuckburgh, 2010: Enhancement of Mesoscale Eddy Stirring at Steering Levels in the South-
707 ern Ocean. *dx.doi.org*, **40** (1), 170–184, doi:10.1175/2009JPO4201.1.
- 708 Abernathey, R. P., and J. Marshall, 2013: Global surface eddy diffusivities derived from satellite al-
709 timetry. *Journal of Geophysical Research: Oceans*, **118** (2), 901–916, doi:10.1002/jgrc.20066.
- 710 Amores, A., O. Melnichenko, and N. Maximenko, 2016: Coherent mesoscale eddies in the North
711 Atlantic subtropical gyre : 3D structure and transport with application to the salinity maximum
712 . *Journal of Geophysical Research: Oceans*, 1–45, doi:10.1002/2016JC012256, URL <http://doi.wiley.com/10.1002/2016JC012256>.
- 714 Bingham, F. M., J. Busecke, A. L. Gordon, C. F. Giulivi, and Z. Li, 2014: The North Atlantic sub-
715 tropical surface salinity maximum as observed by Aquarius. *Journal of Geophysical Research:*
716 *Oceans*, **119** (11), 7741–7755, doi:10.1002/2014JC009825.
- 717 Boccaletti, G., R. Ferrari, A. Adcroft, D. Ferreira, and J. Marshall, 2005: The vertical struc-
718 ture of ocean heat transport. *Geophysical research letters*, **32** (10), L10 603, doi:10.1029/
719 2005GL022474.
- 720 Bryan, F., and S. Bachman, 2014: Isohaline salinity budget of the North Atlantic salinity maxi-
721 mum. *dx.doi.org*, **45** (3), 724–736, doi:10.1175/JPO-D-14-0172.1.
- 722 Busecke, J., A. L. Gordon, Z. Li, F. M. Bingham, and J. Font, 2014: Subtropical surface layer
723 salinity budget and the role of mesoscale turbulence. *Journal of Geophysical Research: Oceans*,
724 **119** (7), 4124–4140, doi:10.1002/2013JC009715.

- 725 Chelton, D. B., R. A. DeSzeke, M. G. Schlax, K. El Naggar, and N. Siwertz, 1998: Geographical
726 Variability of the First Baroclinic Rossby Radius of Deformation. *J Phys Oceanogr*, **28** (3),
727 433–460, doi:10.1175/1520-0485(1998)028<433:GVOTFB>2.0.CO;2.
- 728 Durack, P. J., 2015: Ocean Salinity and the Global Water Cycle. *Oceanography*, **28** (1), 20–31,
729 doi:10.5670/oceanog.2015.03.
- 730 Durack, P. J., and S. E. Wijffels, 2010: Fifty-Year Trends in Global Ocean Salinities and Their
731 Relationship to Broad-Scale Warming. *Journal of Climate*, **23** (16), 4342–4362, doi:10.1175/
732 2010JCLI3377.1.
- 733 Farrar, J. T., L. Rainville, A. J. Plueddemann, and W. S. Kessler, 2015: Salinity and temperature
734 balances at the SPURS central mooring during fall and winter. *Oceanography*, doi:10.5670/
735 oceanog.2015.06.
- 736 Forget, G., J. M. Campin, P. Heimbach, C. N. Hill, and R. M. Ponte, 2015: ECCO version 4: an
737 integrated framework for non-linear inverse modeling and global ocean state estimation. *Geo-
738 scientific Model Development Discussions*, **8** (5), 3653–3743, doi:10.5194/gmd-8-3071-2015.
- 739 Fox-Kemper, B., R. Lumpkin, and F. O. Bryan, 2013: Lateral transport in the ocean interior. *Ocean
740 Circulation and Climate: A 21st century perspective*, **103**, 185–209.
- 741 Gordon, A., and C. Giulivi, 2008: Sea Surface Salinity Trends over Fifty Years Within the Sub-
742 tropical North Atlantic. *Oceanography*, **21** (1), 20–29.
- 743 Gordon, A. L., 2016: The marine hydrological cycle: The ocean's floods and droughts. *Geophysi-
744 cal research letters*, doi:10.1002/2016GL070279.

- 745 Gordon, A. L., and C. F. Giulivi, 2014: Ocean eddy freshwater flux convergence into the
746 North Atlantic subtropics. *Journal of Geophysical Research*, **119** (6), 3327–3335, doi:10.1002/
747 2013JC009596.
- 748 Gordon, A. L., C. F. Giulivi, J. Busecke, and F. M. Bingham, 2015: Differences among subtropical
749 surface salinity patterns. *Oceanography*, **28** (1), 1–30, doi:10.5670/oceanog.2015.02.
- 750 Groeskamp, S., B. M. Sloyan, J. D. Zika, and T. J. McDougall, 2017: Mixing inferred from
751 an ocean climatology and surface fluxes. *Journal of Physical Oceanography*, doi:10.1175/
752 JPO-D-16-0125.1.
- 753 Held, I. M., and B. J. Soden, 2006: Robust responses of the hydrological cycle to global warming.
754 *Journal of Climate*, **19** (21), 5686–5699, doi:10.1175/JCLI3990.1.
- 755 Huffman, G. J., and Coauthors, 2010: The Global Precipitation Climatology Project (GPCP) Com-
756 bined Precipitation Dataset. *Bulletin of the American Meteorological Society*, **78** (1), 5–20, doi:
757 10.1175/1520-0477(1997)078<0005:TGPCPG>2.0.CO;2.
- 758 Johnson, B. K., F. O. Bryan, S. A. Grodsky, and J. A. Carton, 2016: Climatological Annual Cycle
759 of the Salinity Budgets of the Subtropical Maxima. *Journal of Physical Oceanography*, 15–
760 0202, doi:10.1175/JPO-D-15-0202.1.
- 761 Klocker, A., and R. Abernathey, 2014: Global patterns of mesoscale eddy properties and diffusiv-
762 ities. *Journal of Physical Oceanography*, doi:10.1175/JPO-D-13-0159.1.
- 763 Lee, M.-M., A. J. G. Nurser, A. C. Coward, and B. A. De Cuevas, 2009: Effective Eddy Diffu-
764 sivities Inferred from a Point Release Tracer in an Eddy-Resolving Ocean Model. *Journal of*
765 *Physical Oceanography*, **39** (4), 894–914, doi:10.1175/2008JPO3902.1.

- 766 Lindstrom, E., F. Bryan, and R. Schmitt, 2015: SPURS: Salinity Processes in the Upper-ocean
767 Regional StudyThe North Atlantic Experiment. *Oceanography*, doi:10.5670/oceanog.2015.01.
- 768 Marshall, J., A. Adcroft, C. Hill, L. Perelman, and C. Heisey, 1997: A finitevolume, incompress-
769 ible Navier Stokes model for studies of the ocean on parallel computers. *Journal of Geophysical*
770 *Research: Oceans (19782012)*, **102** (C3), 5753–5766, doi:10.1029/96JC02775.
- 771 Marshall, J., D. Jamous, and J. Nilsson, 1999: Reconciling thermodynamic and dynamic methods
772 of computation of water-mass transformation rates. *Deep Sea Research Part I: Oceanographic*
773 *Research Papers*, **46** (4), 545–572, doi:10.1016/S0967-0637(98)00082-X.
- 774 Marshall, J., E. Shuckburgh, H. Jones, and C. Hill, 2006: Estimates and Implications of Surface
775 Eddy Diffusivity in the Southern Ocean Derived from Tracer Transport. *Journal of Physical*
776 *Oceanography*, **36** (9), 1806–1821, doi:10.1175/JPO2949.1.
- 777 Nakamura, N., 1996: Two-dimensional mixing, edge formation, and permeability diagnosed in
778 an area coordinate. *Journal of the Atmospheric Sciences*, **53** (11), 1524–1537, doi:10.1175/
779 1520-0469(1996)053<1524:TDMEFA>2.0.CO;2.
- 780 O'Connor, B. M., R. A. Fine, and D. B. Olson, 2005: A global comparison of subtropical un-
781 derwater formation rates. *Deep Sea Research Part I: Oceanographic Research Papers*, doi:
782 10.1016/j.dsr.2005.01.011.
- 783 Ponte, R. M., and N. T. Vinogradova, 2016: An assessment of basic processes controlling mean
784 surface salinity over the global ocean. *Geophysical research letters*, **43** (13), 7052–7058, doi:
785 10.1002/2016GL069857.
- 786 Qu, T., S. Gao, and I. Fukumori, 2011: What governs the North Atlantic salinity maximum in a
787 global GCM? *Geophysical Research Letters*, **38** (7), 1–6, doi:10.1029/2011GL046757.

- 788 Rypina, I. I., I. Kamenkovich, P. S. Berloff, and L. J. Pratt, 2012: Eddy-Induced Particle Dispersion
789 in the Near-Surface North Atlantic. *Journal of Physical Oceanography*, **42** (12), 2206–2228,
790 doi:10.1175/JPO-D-11-0191.1.
- 791 Schanze, J. J., R. W. Schmitt, and L. L. Yu, 2010: The global oceanic freshwater cycle: A
792 state-of-the-art quantification. *Journal of Marine Research*, **68** (3), 569–595, doi:10.1357/
793 002224010794657164.
- 794 Schmidtko, S., G. C. Johnson, and J. M. Lyman, 2013: MIMOC: A global monthly isopycnal
795 uperocean climatology with mixed layers. *Journal of Geophysical Research: Oceans*, 1–15,
796 doi:10.1002/jgrc.20122.
- 797 Schmitt, R. W., 2008: Salinity and the Global Water Cycle. *Oceanography*, **21** (1).
- 798 Schmitt, R. W., and A. Blair, 2015: A river of salt. *Oceanography*, doi:10.5670/oceanog.2015.04.
- 799 Schott, F. A., J. P. McCreary, and G. C. Johnson, 2004: Shallow overturning circulations of the
800 tropical subtropical oceans. *Earth's Climate*, **147**, 261–304.
- 801 Vinogradova, N. T., and R. M. Ponte, 2013: Clarifying the link between surface salinity and fresh-
802 water fluxes on monthly to interannual time scales. *Journal of Geophysical Research: Oceans*,
803 **118** (6), 3190–3201, doi:10.1002/jgrc.20200.
- 804 Walin, G., 1977: A theoretical framework for the description of estuaries. *Tellus*, **29** (2), 128–136,
805 doi:10.3402/tellusa.v29i2.11337.
- 806 Wüst, G., 1936: Oberflächensalzgehalt, Verdunstung und Niederschlag auf dem Weltmeere nebst
807 Bemerkungen zum Wasserhaushalt der Erde. *Norbert Krebs, Stuttgart*.
- 808 Yu, L., X. Jin, and R. A. Weller, 2008: Multidecade Global Flux Datasets from the Objectively
809 Analyzed Air-sea Fluxes (OAFlux) Project: Latent and sensible heat fluxes, ocean evaporation,

⁸¹⁰ and related surface meteorological variables. OAFlux Project Technical Report. OA-2008-01,
⁸¹¹ 64pp. (2008).

812 **LIST OF TABLES**

813	Table 1. List of initial conditions and corresponding suffixes used in the text. Data	40
814	sources are given in parentheses in the last column. See section 2 for details.		
815	Table 2. Mean Results; The columns show the results from the 'MIMOC mean' exper-		
816	iment. In each column (basin) the values are calculated according to the refer-		
817	ence salinities from (Gordon et al. 2015) (bold font) and (Johnson et al. 2016)		
818	(regular font). The rank for each basin is given in parentheses after the value.		
819	From top to bottom: The Transformation rate (TFR); The surface forcing com-		
820	pensation from the volume budget (SFC); The surface forcing compensation		
821	from the Salinity budget (SFC_S); The SFC estimate from the salinity budget		
822	over the full depth from (Johnson et al. 2016) ($SFC_{S,FullDepth}$) and a compa-		
823	rison between (SFC_S) and ($SFC_{S,FullDepth}$) (Mixed Layer vs. interior). Note		
824	that for the last row results are derived for both reference salinities by dividing		
825	both values for (SFC_S) by the single results from (Johnson et al. 2016). Please		
826	note the bold values in the last row are comparing values where the reference		
827	salinities are not equal. For details see text.		41

Group suffix	Individual suffix	Initial SSS condition
-	mean	full time mean (MIMOC)
	jan	climatological January (MIMOC)
	feb	climatological February (MIMOC)
monthly
	nov	climatological November (MIMOC)
	dec	climatological December (MIMOC)
	ECCO 1992	annual mean 1992 (ECCO)
	ECCO 1993	annual mean 1993 (ECCO)
annual, ECCO
	ECCO 2010	annual mean 2013 (ECCO)
	ECCO 2011	annual mean 2014 (ECCO)
	ARGO 2006	annual mean 2006 (APDRC)
	ARGO 2007	annual mean 2007 (APDRC)
annual, ARGO
	ARGO 2013	annual mean 2013 (APDRC)
	ARGO 2014	annual mean 2014 (APDRC)

828 TABLE 1. List of initial conditions and corresponding suffixes used in the text. Data sources are given in
 829 parentheses in the last column. See section 2 for details.

Basin	NA		SA		NP		SP		SI	
S _{ref}	37.2	37.0	37.1	37.0	35.2	35.2	36.3	36.1	35.8	35.6
TFR [Sv]	2.00 (3)	1.40 (2)	1.48 (2)	1.52 (3)	3.46 (5)	3.46 (5)	1.20 (1)	1.02 (1)	3.43 (4)	2.15 (4)
SFC [%]	19 (4)	14 (2)	19 (3)	18 (5)	16 (2)	16 (4)	10 (1)	7 (1)	25 (5)	15 (3)
SFC _S [%]	15 (4)	16 (4)	17 (5)	17 (5)	13 (3)	13 (2)	11 (1)	9 (1)	11 (2)	15 (3)
SFC _{S,FullDepth} [%]		55 (3)		46 (2)		60 (4)		41 (1)		70 (5)
Mixed Layer vs Interior	27 (4)	29 (4)	36 (5)	37 (5)	22 (2)	22 (1)	26 (3)	23 (3)	16 (1)	22 (2)

830 TABLE 2. Mean Results; The columns show the results from the 'MIMOC mean' experiment. In each column
 831 (basin) the values are calculated according to the reference salinities from (Gordon et al. 2015) (bold font) and
 832 (Johnson et al. 2016) (regular font). The rank for each basin is given in parentheses after the value. From top to
 833 bottom: The Transformation rate (TFR); The surface forcing compensation from the volume budget (SFC); The
 834 surface forcing compensation from the Salinity budget (SFC_S); The SFC estimate from the salinity budget over
 835 the full depth from (Johnson et al. 2016) ($SFC_{S,FullDepth}$) and a comparison between (SFC_S) and ($SFC_{S,FullDepth}$)
 836 (Mixed Layer vs. interior). Note that for the last row results are derived for both reference salinities by dividing
 837 both values for (SFC_S) by the single results from (Johnson et al. 2016). Please note the bold values in the last
 838 row are comparing values where the reference salinities are not equal. For details see text.

LIST OF FIGURES

- Fig. 1.** Schematic illustrating the investigated processes. Orange surfaces symbolize lines of constant surface salinity scaled by the mean Mixed Layer Depth (MLD). The smooth initial condition in each experiment (a) gets stirred by mesoscale velocities (blue arrows), which enhances the diffusive flux (black arrows) across the contour (b). The integrated flux across a closed contour (indicated by wavy gray arrows in c) leads to the destruction of salty water masses within the contour - the transformation rate (TFR; indicated by dotted arrows in c). 43

Fig. 2. Mean SSS from MIMOC (upper) and surface diffusivities reproduced from Abernathey et al. 2013 (lower) in color. In the upper plot the black contour represents the S_{ref} contour for each basin based on Gordon et al. (2015) for the $MIMOC_{mean}$ initial condition. In the lower box the same salinity is shown for all used initial conditions (see Tab. 1 for reference). Black boxes indicate regional domains used in this study. 44

Fig. 3. Time averaged diagnostics in salinity space. All computed from ' $MIMOC_{mean}$ ' experiment. a): Transformation Rates (TFR) by Eddy Mixing . b): Surface Forcing Compensation. c): Effective Diffusivities (K_{eff}). d): Mean Transformation Rates by Surface Forcing. Colors indicate ocean basin and the y axis is the salinity of the bounding isohaline. The y-axis represents the difference from the S_{ref} value (Figure 2) in each basin, with positive values representing isohalines toward the center of the SSS-max. When the area within an isohaline is smaller than 100 grid boxes the line is dashed. 45

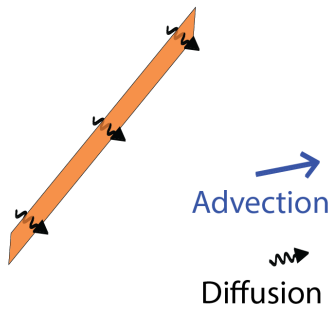
Fig. 4. Seasonal cycle (left column) and interannual variability (right column) of Transformation Rate [Sv] on S_{ref} . The sign is reversed, with positive values indicating destruction of salty water masses. Colors indicate different experiments (see Table 1). Left column: Seasonal cycle. Blue indicates TFR_{mean} black $TFR_{combined}$ and gray lines are all $TFR_{monthly}$ experiments. Right column: interannual record, derived by pre-averaging every 4 months and smoothing with a 1.5 year Gaussian window. Colors as before with gray indicating all experiments with annual initial conditions (Table 1). Thick black and grey lines indicates $TFR_{combined}$ derived from experiments with annually averaged initial conditions from ECCO and ARGO respectively, for more details see text. K_{eff} (red) is displayed in all plots normalized by the mean and std of TFR_{mean} for comparison. 46

Fig. 5. Effective Diffusivities for S_{ref} . $K_{eff,mean}$ (thick line) and the std of the monthly (left) and annual (right) experiments (indicated by thin lines) are shown for all basins (color) for the seasonal (left) and interannual (right) signal, processed identical to the TFR (see Figure 4). 47

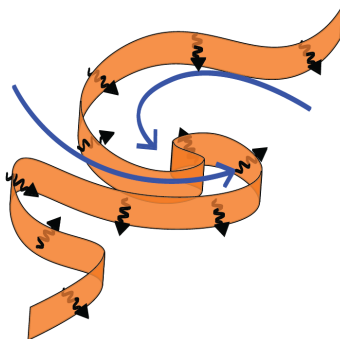
Fig. A1. Root mean square error due to reset procedure. Values are shown for the respective basins and the various time frames considered (color see legend). For details see text. 48

Fig. A2. Schematic for the construction of the 'combined monthly' experiment. Each colored row is an experiment with quasi-constant intial conditions (see Table 1 and text for details). Each box represents a month in the full time record (extended for multiple years indicated by the dots on the right). The combined experiment is constructed by concatenating the time series from the respective experiment for each month(dark boxes). 49

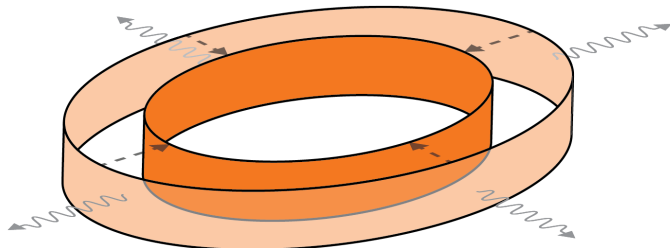
a) Smooth surface
low K_{eff}
low integrated flux



b) Contorted surface due to stirring
high K_{eff}
high integrated flux

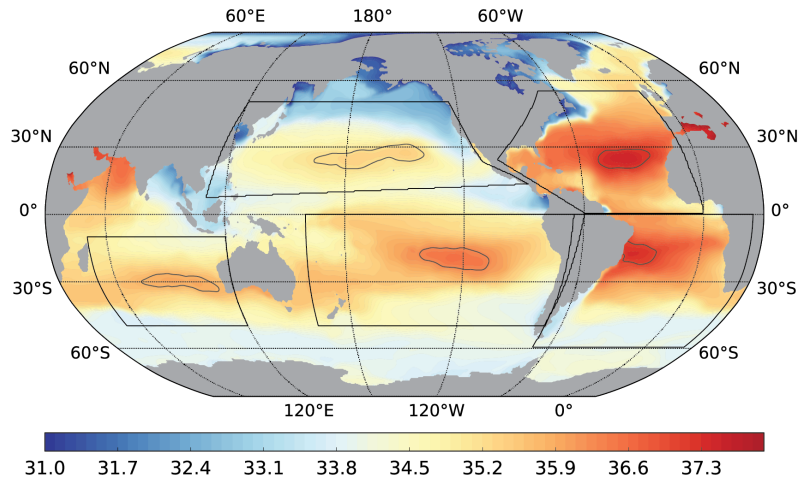


c) Area within isohalines shrinks due to integrated flux (TFR)



878 FIG. 1. Schematic illustrating the investigated processes. Orange surfaces symbolize lines of constant surface
879 salinity scaled by the mean Mixed Layer Depth (MLD). The smooth initial condition in each experiment (a) gets
880 stirred by mesoscale velocities (blue arrows), which enhances the diffusive flux (black arrows) across the contour
881 (b). The integrated flux across a closed contour (indicated by wavy gray arrows in c) leads to the destruction of
882 salty water masses within the contour - the transformation rate (TFR; indicated by dotted arrows in c).

Mean Sea Surface Salinity from Argo



Log10 of Surface Diffusivities

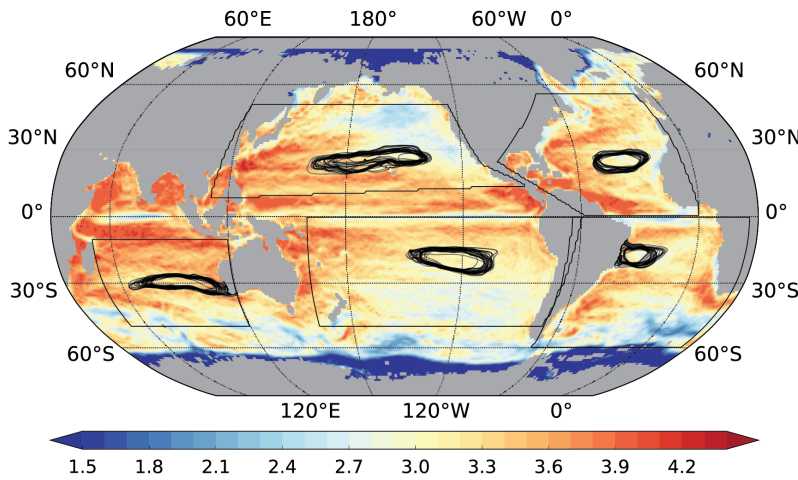


FIG. 2. Mean SSS from MIMOC (upper) and surface diffusivities reproduced from Abernathey et al. 2013 (lower) in color. In the upper plot the black contour represents the S_{ref} contour for each basin based on Gordon et al. (2015) for the $MIMOC_{mean}$ initial condition. In the lower box the same salinity is shown for all used initial conditions (see Tab. 1 for reference). Black boxes indicate regional domains used in this study.

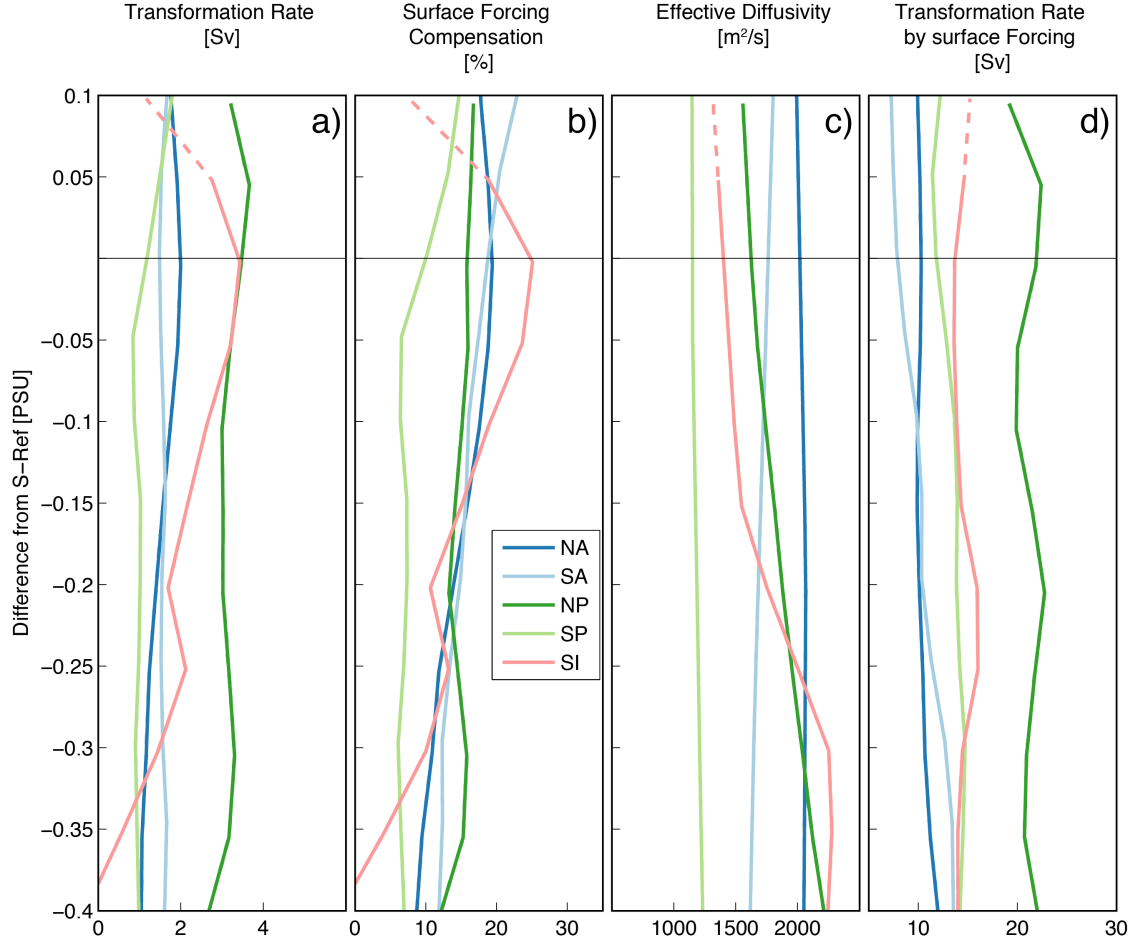
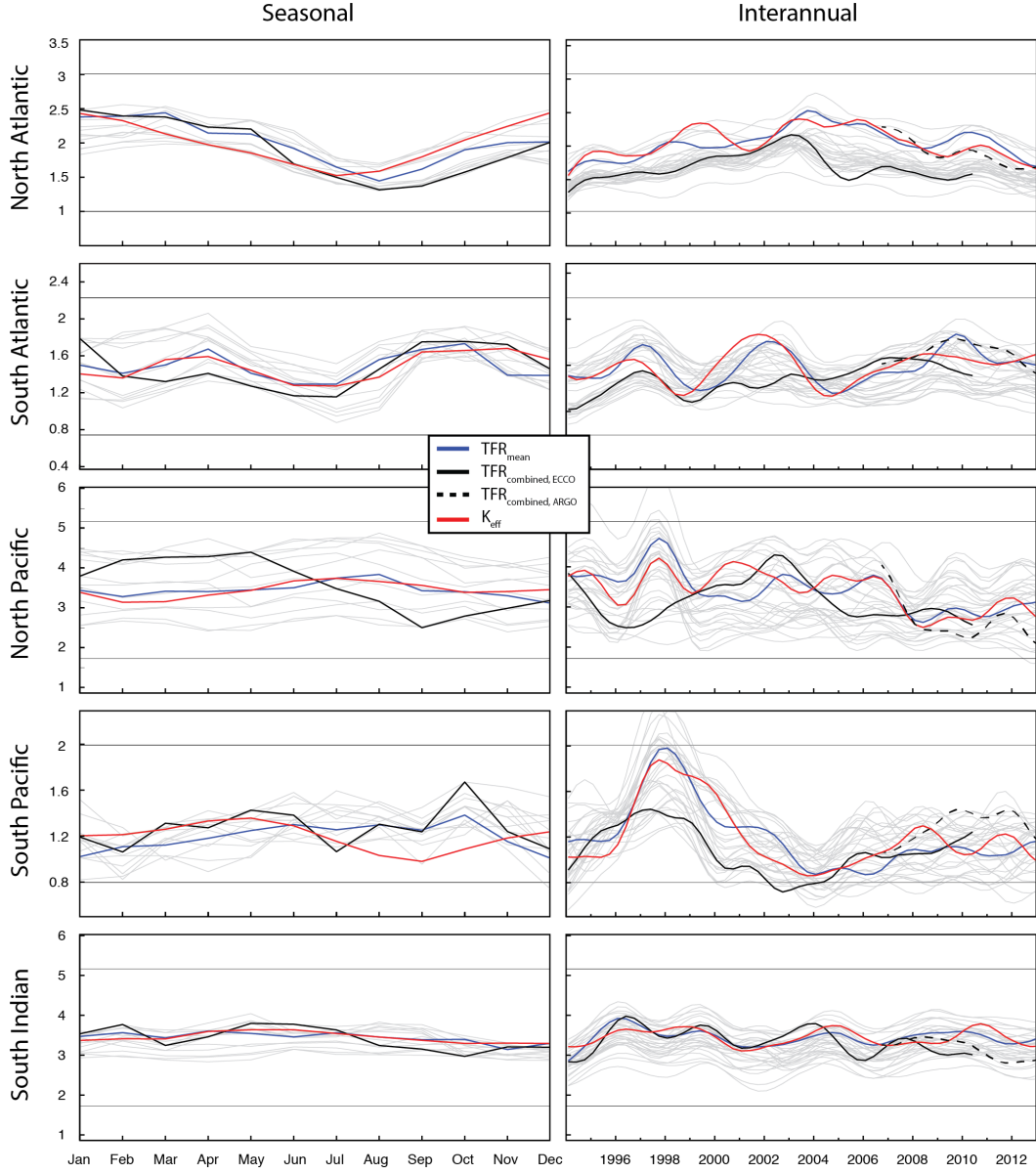
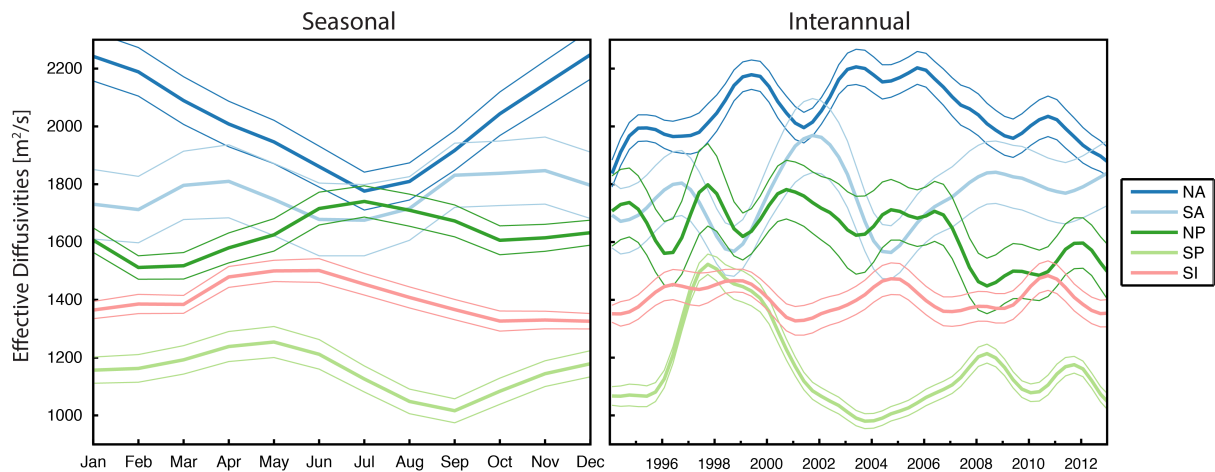


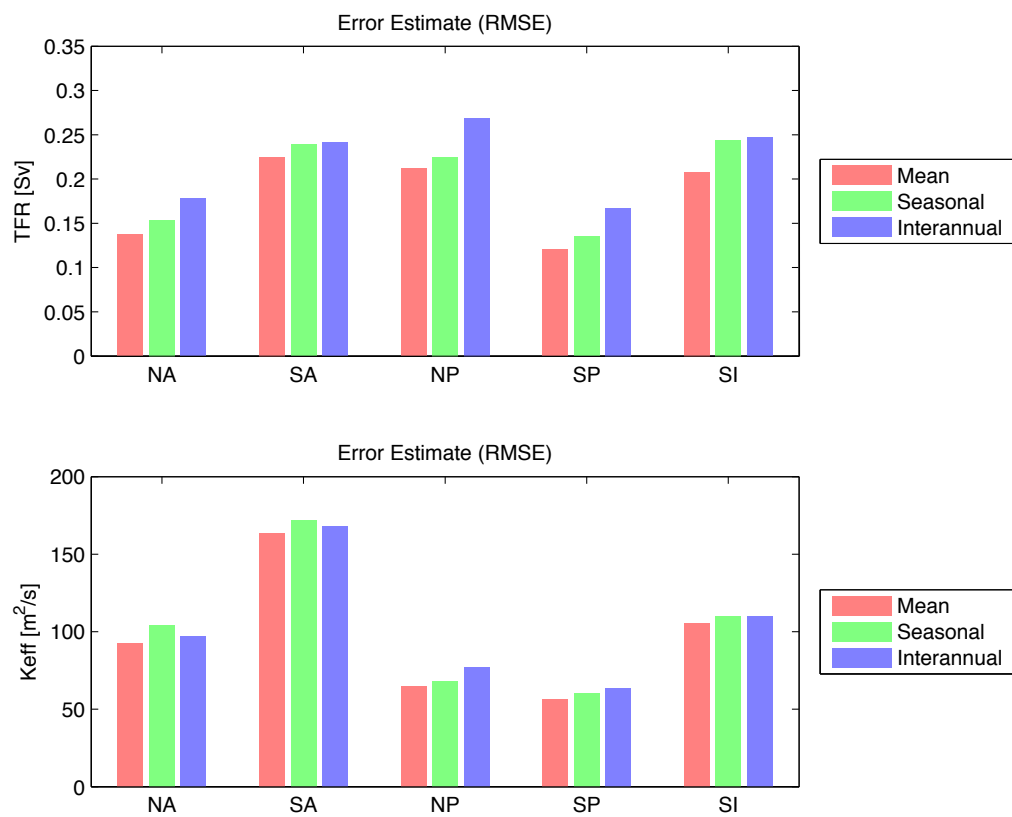
FIG. 3. Time averaged diagnostics in salinity space. All computed from '*MIMOC_{mean}*' experiment. a): Transformation Rates (*TFR*) by Eddy Mixing . b): Surface Forcing Compensation. c): Effective Diffusivities (K_{eff}). d): Mean Transformation Rates by Surface Forcing. Colors indicate ocean basin and the y axis is the salinity of the bounding isohaline. The y-axis represents the difference from the S_{ref} value (Figure 2) in each basin, with positive values representing isohalines toward the center of the SSS-max. When the area within an isohaline is smaller than 100 grid boxes the line is dashed.



893 FIG. 4. Seasonal cycle (left column) and interannual variability (right column) of Transformation Rate [Sv]
 894 on S_{ref} . The sign is reversed, with positive values indicating destruction of salty water masses. Colors indicate
 895 different experiments (see Table 1). Left column: Seasonal cycle. Blue indicates TFR_{mean} black $TFR_{combined}$
 896 and gray lines are all $TFR_{monthly}$ experiments. Right column: interannual record, derived by pre-averaging
 897 every 4 months and smoothing with a 1.5 year Gaussian window. Colors as before with gray indicating all
 898 experiments with annual initial conditions (Table 1). Thick black and grey lines indicates $TFR_{combined}$ derived
 899 from experiments with annually averaged initial conditions from ECCO and ARGO respectively, for more details
 900 see text. K_{eff} (red) is displayed in all plots normalized by the mean and std of TFR_{mean} for comparison.



901 FIG. 5. Effective Diffusivities for S_{ref} . $K_{eff,mean}$ (thick line) and the std of the monthly (left) and annual (right)
902 experiments (indicated by thin lines) are shown for all basins (color) for the seasonal (left) and interannual (right)
903 signal, processed identical to the *TFR* (see Figure 4).



904 Fig. A1. Root mean square error due to reset procedure. Values are shown for the respective basins and the
 905 various time frames considered (color see legend). For details see text.

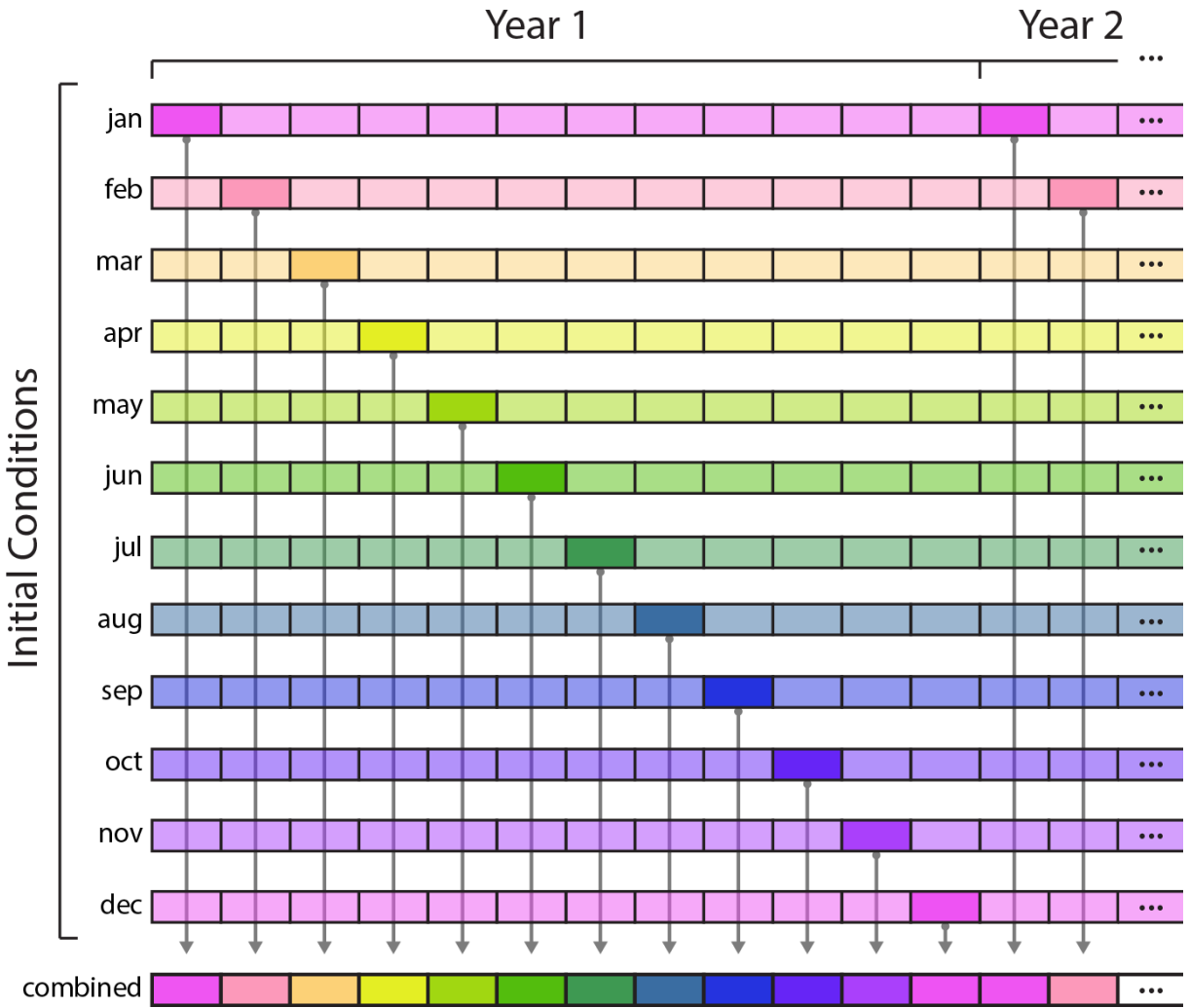


Fig. A2. Schematic for the construction of the 'combined monthly' experiment. Each colored row is an experiment with quasi-constant initial conditions (see Table 1 and text for details). Each box represents a month in the full time record (extended for multiple years indicated by the dots on the right). The combined experiment is constructed by concatenating the time series from the respective experiment for each month (dark boxes).